

Printed in: **Astronomy Report, 2003, v.47, p.186**

Supersoft X-ray Sources. Parameters of Stellar Atmospheres

A. A. Ibragimov¹, V.F.Suleimanov¹, A. Vikhlinin², and N. A. Sakhibullin¹

1 - Kazan State University, Kazan, Tatarstan, Russia

2 - Space Research Institute, Moscow, Russia

Received March 5, 2002; in final form, October 10, 2002

Abstract

ROSAT spectra of 11 supersoft X-ray sources (RX J0439.8-6809, RX J0513.9-6951, RX J0527.8-6954, CAL 87, CAL 83, 1E 0035.4-7230, RX J0048.4-7332, 1E 0056.8-7154, RX J0019.8 +2156, RX J0925.7-4758, AG Draconis) are approximated with theoretical spectra obtained in LTE models for the atmospheres of hot white dwarfs with line blanketing. The confidence intervals of parameters derived from these approximations T_{eff} , $\log g$, N_H , and R^2/d^2 are determined.

The results are compared with predictions for a model with stable/recurrent thermonuclear burning on the white-dwarf surface.

1. Introduction

Supersoft X-ray sources (hereafter "supersoft sources") are a class of X-ray object distinguished by ROSAT observations (Trümper et al. 1991, Hasinger 1994, Kahabka and van den Heuvel, 1997). The main characteristic of these objects is a very soft X-ray spectrum that falls off near 0.5 - 1 keV. Blackbody approximations to the X-ray spectra yield temperatures from 10 to 80 eV. As a rule, the luminosities derived from such approximations are very high ($\sim 10^{38}$ erg/s), and often exceed the Eddington limit for solar-mass objects. The first observations of supersoft sources were obtained by the Einstein Observatory, but ROSAT was the first satellite that was able to distinguish them as a distinct class and detect significant numbers of these sources. Currently, about 60 bright supersoft sources are known, located in our Galaxy, the Magellanic Clouds, the Andromeda galaxy, and NGC 55 (Greiner 2000).

One widely adopted model that can explain the nature of at least classical double supersoft sources is that of van den Heuvel et al. (1992), in which supersoft sources are close binary systems containing a white dwarf and a more massive subgiant secondary that overfills its Roche lobe. If the mass of the latter star is approximately twice the mass of the white dwarf, the accretion onto the white dwarf occurs on the thermal time scale for the secondary at a high rate ($\sim 10^{-7} M_{\odot}/\text{yr}$), which gives rise to stable nuclear burning on its surface, leading to the observed soft X-ray emission. The theoretical possibility of such a situation was predicted in (Paczynski and Zytkov 1977) and subsequently studied in detail by a number of authors (Iben 1982, Nomoto 1982, Fujimoto 1982, Iben and Tutukov 1996).

The spectral energy distribution of such a supersoft source should be described by the theoretical spectrum of a white-dwarf model atmosphere with the appropriate effective temperature T_{eff} , gravitational acceleration g , and chemical composition A (see Section 3). Atmospheres with $T_{\text{eff}} \sim 10^5 - 10^6$ K radiate more efficiently at energies 0.1 - 0.5 keV than a blackbody, so that applying LTE model atmospheres without taking lines into account yielded bolometric luminosities for supersoft sources that were below the Eddington limit for a solar-mass object (Heise et al. 1994).

The X-ray spectra of supersoft sources have been approximated using a variety of theoretical models, from blackbody models to non-LTE models taking line absorption into account (Hartmann et al. 1999). The parameters of most sources have been estimated using LTE models without including the effect of line absorption.

Our goal in the current study was to rereduce series of ROSAT observations of known supersoft sources using a unified method, in order to derive the physical characteristics of these objects in a uniform way, approximating the observed fluxes using theoretical spectra for blanketed (i.e. including the effect of lines) LTE model atmospheres for hot white dwarfs. It is obvious that considering blanketing of non-LTE model atmospheres for hot white dwarfs would be more realistic, but such computations are appreciably more complex and time-consuming (Hubeny and Lanz 1995). In addition, we note that the temperature structures of blanketed non-LTE and LTE model atmospheres are very similar and differ substantially from non-LTE models without line absorption (Anderson 1990). Therefore, we consider blanketed LTE-model atmospheres of hot white dwarfs to be more realistic than non-LTE models without line absorption (Anderson 1990).

Recent high resolution (~ 0.06 Å) calibration observations of the source CAL 83 by the XMM-Newton satellite (Paerels et al 2001) showed that its spectrum is rich in absorption lines. This indicates the photospheric nature of the spectrum and demonstrates that any detailed analysis of the X-ray spectra of these objects obtained by the new generation of space observatories must make use of the method of synthetic spectra.

The full designations of the sources are presented in Table 2. We will use shortened designations consisting only of the first several symbols.

In all, we studied ten supersoft sources. We also present data for AG Dra; although its spectrum is very soft, the resulting parameters are very uncertain and are not interpreted further. The parameters of the two sources RX J0527 and RX J0513 are the first derived using white-dwarf model atmospheres.

2. Data reduction

The sample of sources corresponds to the list of Greiner (2000). A number of objects were excluded due to the absence of satisfactory observations or the exceptional softness of their spectra, which led to very large uncertainties in their parameters (the results for AG Dra demonstrate what occurs in this case). In the end, we used 11 sources and 13 observations in our study.

The spectra of the objects were extracted from a circular region with a radius large enough to include the majority of the photons. Information about the background was extracted from a zone having an area several times larger surrounding the source. To increase the signal-to-noise ratios and obtain a high correspondence to the energy resolution of the detector, the spectral flux densities were recalculated to new energy channels that were broader than the instrumental channels (Table 1).

We estimated the physical parameters of the sources by approximating the observed spectra with theoretical spectra derived from computations of blanketed LTE model atmospheres taking into account interstellar absorption. The free parameters in the fitting were the column density of interstellar hydrogen N_H , the effective temperature of the model atmosphere T_{eff} , and a normalization factor accounting for the geometrical decrease in the flux, R^2/d^2 (R is the source radius and d is the distance to the source). The gravitational acceleration $\log g$ was fixed at a preliminarily determined optimal value (this parameter influences the spectrum much more weakly than the others; see Section 4).

Table 2 presents the main data on the sources and the parameters of the observations used.

3. Method for computing the hot white-dwarf model atmospheres

The model atmospheres were characterized by their effective temperature T_{eff} , surface gravitational acceleration g , and a scaling factor for the abundance of elements heavier than helium A . Solar chemical composition corresponds to $A=1$, and a heavy- element content a factor of ten lower corresponds to $A = 0.1$. We assumed that the atmosphere was stationary and static, and consisted of uniform, planeparallel layers.

The model atmosphere was found numerically, and the distribution of atoms and ions in terms of their excitation and degrees of ionization were determined by the Saha and Boltzmann equations assuming local thermodynamic equilibrium. We used a modified version of the ATLAS5 code of Kurucz (1970). The computations included the 15 most widespread elements (H, He, C, N, O, Ne, Na, Mg, Al, Si, S, Ar, Ca, Fe, Ni). In contrast to the original code of Kurucz, we considered all ionization states. Data on the opacity cross sections were taken from (Verner et al. 1996). We also took into account Thomson scattering on free electrons (Compton effects in the atmospheres of white dwarfs weaken as the gravitational acceleration increases, and do not influence the continuum spectrum (Madej 1994). We included about 1200 of the strongest spectral multiplets and lines (for the ionization states corresponding to the conditions in the atmosphere) selected from the list (Verner et al. 1996), whose effect was determined via direct integration. We took the line profiles to be Voigt profiles broadened by natural damping, the Doppler effect (taking the microturbulent velocity to be 1 km/s), and the Stark effect. The Stark half- width was computed using the simple approximation formula of Kurucz and Furenlid (1979). We used a grid of ~ 8000 points in frequency (from $3 \cdot 10^{13}$ to 10^{21} Hz) and 100 points in depth to solve the radiative-transfer equation using the method of Auer (1976) for three angles. The upper boundary condition assumed the absence of a rising flux at the first surface point. We used a diffusion approximation as a lower boundary condition. The temperature structure of the atmosphere was computed using a temperature-correction method.

In some high-lying points in the atmosphere (which exert virtually no influence on the emergent flux), the radiation pressure can exceed the gravitational force. Physically, this implies the presence of a stellar wind from the surface of the white dwarf. However, the study of this wind falls outside the framework of the problem at hand, and we will ignore its effect.

4. Results of the computations

We computed a grid of model white-dwarf atmospheres with solar chemical composition (Anders and Grevesse 1989) and with effective temperatures $5 \cdot 10^4 - 1.3 \cdot 10^6$ K in steps of 10^4 K and surface gravities $\log g = 7.0 - 9.5$ in steps of 0.5 for comparison with the observations. We computed only the models that did not exceed the Eddington limit, i.e., with $\log g > \log g_E$. This limiting surface gravity $\log g_E$ is specified by the relation

$$\log g_E = 4.88 + 4 \log T5, \quad (1)$$

where $T5 = T_{\text{eff}}/10^5$ K.

The results of the computations are illustrated in Fig. 1. Figure 1a shows the temperature structures of the blanketed and unblanketed models. Figure 1b shows the difference between the model spectra without lines (dashed) and with lines (solid). This difference is more clearly

visible in Fig. 1c, which shows the spectra averaged over intervals of 10 eV. The flux of the blanketed model is lower at high energies and higher at softer energies than that of the unblanketed model, reflecting the differences in their temperature structures. There are also local dips associated with the presence of large numbers of strong lines in these regions. Note that the uncertainty associated with our poor knowledge of the magnitude of the Stark effect for the spectral lines does not significantly influence the resulting spectral energy distribution.

Figure 2 shows the dependence of the spectra on variations of the model parameters: effective temperature (Fig. 2a), surface gravity (Fig. 2b), and heavy- element abundance (Fig. 2c). At energies above 0.5 keV, variations in the slope and overall flux of the spectra are most appreciable in the presence of variations of the effective temperature. Variations of $\log g$ influence the overall redistribution of energy much more weakly, and variations of the chemical composition are manifest only via differing values for absorption jumps.

5. Fitting technique

The PSPC instrument on ROSAT has the following characteristics at soft energies. The energy resolution of the detector ($\Delta E/E$) to 0.5 keV is about film shielding the instrument. In addition, absorption 90%. The detector has no sensitivity near 0.4 keV in the interstellar medium exerts a large influence at since photons with this energy are absorbed in the these energies. If there are no photons with energies higher than 0.5 keV in an observed spectrum, variations in the interstellar absorption may be compensated by the joint influence of the normalization for the dilution of the flux and the effective temperature, which affects the slope of the spectrum. As a result, various combinations of these three parameters can yield statistically similar results. This is usually visible in a plot of confidence-level contours in the $N_H - T_{\text{eff}}$ plane (curves bounding zones within which the true parameter value is located with some probability) as a characteristic region of possible T_{eff} and N_H values (Fig. 3). As a rule, the upper left part of this zone is consistent with the Galactic value of N_H in the specified direction (we will call this the Galactic N_H value) and yields plausible luminosities for the source.

In connection with this, we estimated the errors in T_{eff} and the normalization when limiting the column density N_H in the region of most plausible parameter values. We adopted the extreme values of the errors of T_{eff} and the normalization for two fixed values of N_H for the boundary values delimiting this region. We first determined the 90% probability boundaries for N_H . Then, we determined the errors in the two other parameters for two values of N_H – the minimum value of N_H and either the maximum value of N_H or double best fit, depending on which turned out to be closer to the best approximation. Observations for which errors were derived in this way are denoted in Tables 3 and 4 by the letters A and B in the type of errors column. Statistically, these errors yield a probability of about 98% that the true value is within the error interval.

For several sources, the parameters were well constrained in the zone corresponding to the best-fit approximation. This is because the data for these sources were fairly hard, so that either the cutoff in their spectra is beyond 0.5 keV (RX J0513) or the maximum observed flux occurs at 0.7 – 0.9 keV (CAL 87 and RX J0925). In this case, we did not use the error-estimation method described above, and the parameter errors were calculated using the usual statistical criteria ($\chi^2 = 2.71$, 90% probability, type C in Tables 3 and 4).

Given the complexity of accurately estimating parameters, we attempted to determine the most general bounds for the possible parameter values. Most often, due to the impossibility of separating the influences of individual parameters, the magnitude of χ^2 remained virtually

unchanged for any value of the surface gravity; however, different effective temperatures were naturally obtained for different surface gravities. Therefore, we present two approximations for nearly all the sources, corresponding to the lower and upper bounding values of the surface gravity.

In addition, very often, very broad limits for the column density N_H were allowed statistically. Our analysis (Section 6) showed that the Galactic column density (Dickey and Lockman 1990) is located within the confidence intervals for most of the sources (located in the Large and Small Magellanic Clouds). Accordingly, we have included approximations for the source parameters obtained by fixing the column density to be the Galactic value (the errors were calculated in the usual way, error type C).

6. Discussion

The approximation results are shown in Tables 3 and 4, which contain the approximation data for $\log g = 7.5$ and 9.5, and Tables 5 and 6, which contain the data for these surface gravities and the Galactic value of N_H . Figure 3 depicts the spectra and confidence contours for the surface gravities used in the analyses for two sources.

Figure 4 compares our results with the data of other authors. Figure 4a shows such a comparison for the effective temperatures. Our data for the minimum $\log g$ are shown for all the sources; for RX J0439, RX J0527, CAL 83, and 1E 0035, we have used the approximation with the Galactic N_H value, while N_H has been left as a free parameter for the other sources. Overall, the agreement is good, though we should point out a number of features.

First, the temperatures for RX J0527 and RX J0513 are approximately 100 000 K higher than those determined by other authors based on approximations of their spectra using Planck functions. Second, for the limiting values of T_{eff} for the two hardest sources CAL 87 and RX J0925, we used temperatures derived from non-LTE models (lower bounds) and unblanketed LTE models (upper bounds) (Hartmann et al 1999, Hartmann and Heise 1997). We can see that the non-LTE values are lower and the LTE values (for the non blanketed models) higher than our values. The remaining sources approximated by non blanketed LTE models also display somewhat higher temperatures than those we derived. Consequently, we conclude that including the effect of lines in the LTE models for the white-dwarf atmospheres leads to lower temperatures for the supersoft sources.

Figure 4b compares our values for N_H in the directions of the sources with previously published values. We adopted the extreme values from the literature data as the limiting values of N_H . If they were known, we used independent values of N_H derived from optical and ultraviolet observations. The figure shows our resulting values for the minimum $\log g$.

We used the data of the Greiner's catalog (2000), as well as from the following papers: 1E 0056 - (Kahabka et al. 1994) (N_H), RX J0048 - (Kahabka et al. 1994), 1E 0035 - (Kahabka et al. 1999), RX J0019 - (Beuermann et al 1996), RX J0925 - (Motch et al. 1994) (N_H).

The gravitational acceleration is poorly constrained. We were able to fix it well only for the three sources with the highest temperatures: RX J0925, CAL 87 (the only possible value for them is $\log g = 9.5$), and RX J0513 ($\log g = 8.4 \pm 0.04$, errors shown are). The errors in their $\log g$ values in Fig. 5 were estimated to be ± 0.5 . For the remaining sources, values of $\log g$ from the entire range of parameters for our model grid are statistically allowed. However, the model of van den Heuvel et al. (1992) predicts a rigorous relation between T_{eff} and $\log g$, according to which stable hydrogen burning is possible without an appreciable increase in the white-dwarf radius only within a rather narrow range of accretion rates, called the stable-burning strip (SBS) (Nomoto 1982, Fujimoto 1982, Iben and Tutukov 1996). The edges of

the SBS depend on the mass of the white dwarf. When the accretion rate \dot{M} is lower, matter will accumulate on the surface of the white dwarf, with subsequent explosive burning and the ejection of the accreting envelope (novae, recurrent novae, and symbiotic novae). At higher values of \dot{M} , there will be continuous stable hydrogen burning with a luminosity close to the Eddington luminosity. The excess matter will be blown out by the optically thick wind from the white-dwarf surface, leading to an increase in the effective radius of the photosphere and a decrease in the effective temperature (Kato 1996). Using the theoretical relation between the mass and radius of a white dwarf (Popham and Narayan 1995), we can reflect the SBS from the $\dot{M} - M$ (Fujimoto 1982) to the $T_{\text{eff}} - \log g$ (van Teeseling et al. 1996) plane. The SBS, Eddington limit, and positions of the sources in these coordinates are shown in Fig. 3. The three sources with well-defined values of $\log g$ lie inside the SBS (within the errors in the parameters). The temperatures of the remaining sources are also consistent with the SBS for the case of the minimum allowed surface gravity ($\log g = 7.5 - 8$).

The computations of models for white dwarfs with stable surface thermonuclear burning predict an increase in the photospheric radius in the SBS by a factor of two to three compared with the radius of a cool white dwarf (Iben 1982, Fujimoto 1982). However, using source sizes exceeding the radius of a cool white dwarf of the given mass by a factor of two when reflecting the stable-burning strip onto the $T_{\text{eff}} - \log g$ plane only leads to a shift of the strip downward to the left along the strip itself and the Eddington limit. Therefore, in this case, the conclusions drawn above that the sources are located in the stable-burning strip remain valid.

7. Conclusion

We have carried out an analysis of archival ROSAT observations of 11 known supersoft X-ray sources. We have derived the atmospheric parameters T_{eff} and $\log g$ for these sources by approximating their spectra using computed theoretical spectra for blanketed LTE models of hot white-dwarf atmospheres. The resulting parameter values are in agreement with values published previously.

In the next our paper (Suleimanov and Ibragimov 2003), we will carry out an analysis of the parameters obtained from the point of view of their consistency with the theory of stable/recurrent burning; luminosity, mass, and radius estimates for seven sources; and a discussion of the effective temperature - mass relation.

8. Acknowledgments

This work was supported by the Russian Foundation for Basic Research (project N 99-02-17488 and 02-02-17174). A. A. Ibragimov thanks the High-energy Astrophysics Department of the Space Research Institute of the Russian Academy of Sciences for hospitality during the time the work was being carried out.

References

- E. Anders and N. Grevesse, *Geochim. Cosmochim. Acta* 1989, 53, 197
- L. Anderson, *Astron. Soc. Pac. Conf. Ser.* 1990, 77
- L. Auer, *J. Quant. Spectrosc. Radiat. Transf.* 1976, 16, 931
- K. Beuermann, K. Reinsch, H. Barwig, et al., *Astron. Astrophys.* 1995, 294, L1
- J. Dickey and F. Lockman, *Ann. Rev. Astron. Astrophys.* 1990, 28, 215
- J. Greiner, *New Astron.* 2000, 5, 137
- M. Fujimoto, *Astrophys. J.* 1982, 257, 767

H. Hartmann and J. Heise, *Astron. Astrophys.* 1997, 322, 591

H. Hartmann, J. Heise, P. Kahabka, C. Motch, and A. Parmar, *Astron. Astrophys.* 1999, 346, 125

G. Hasinger, in *Reviews in Modern Astronomy*, Ed. by G. Klare 1994, 7, 129

J. Heise, A. van Teeseling, and P. Kahabka, *Astron. Astrophys.* 1994, 288, L45

I. Hubeny and T. Lanz, *Astrophys. J.* 1995, 439, 875

I. Iben, *Astrophys. J.* 1982, 259, 244

I. Iben and A. V. Tutukov, *Astrophys. J. Suppl. Ser.* 1996, 105, 145

P. Kahabka, W. Pietsch, and G. Hasinger, *Astron. Astrophys.* 1994, 288, 538

P. Kahabka and van den E. P. J. Heuvel, *Ann. Rev. Astron. Astrophys.* 1997, 35, 69

P. Kahabka, A. Parmar, and H. Hurtmann, *Astron. Astrophys.* 1999, 346, 453

M. Kato, in *Supersoft X-Ray Sources*, Ed. by J. Greiner; *Lect. Notes Phys.* 1996, 472, 15

R. Kurucz, *Smithson. Astrophys. Obs. Spec. Rep.* 1970, 309, 1

R. Kurucz and I. Furenlid, *Smithson. Astrophys. Obs. Spec. Rep.* 1979, 387, 1

J. Madej, *Astron. Astrophys.* 1994, 286, 515

C. Motch, G. Hasinger, and W. Pietsch, *Astron. Astrophys.* 1994, 284, 827

K. Nomoto, *Astrophys. J.* 1982, 253, 798

B. Paczynski and A. Zytkow, *Astrophys. J.* 1978, 222, 604

F. Paerels, A. Rasmussen, H. Hurtmann, et al., *astro-ph/0011038* (2000).

R. Popham and R. Narayan, *Astrophys. J.* 1995, 442, 337

V. F. Suleimanov and A. A. Ibragimov, *Astron. Rep.* 2003, 47, 197

J. Trümper, G. Hasinger, and B. Aschenbach, et al., *Nature*, 1991, 349, 579

E. P. J. van den Heuvel, D. Bhattacharya, K. Nomoto, and S. Rappaport, *Astron. Astrophys.* 1992, 262, 97

A. van Teeseling, J. Heise, and P. Kahabka, in *IAU Symp. 165: Compact Stars in Binaries*, Ed. by J. van Paradijs, E. P. J. van den Heuvel, E. Kuulkers, et al. (Kluwer Academic, Dordrecht, 1996), p. 445.

D. A. Verner, G.H. Ferland, K.T. Korista, and D. G. Yakovlev, *Astrophys. J.* 1996, 465, 487

D. A. Verner, E. M. Verner, and L. J. Ferland, *Bull. Am. Astron. Soc.* 1996, 188, 54.18

Table 1: Grouping of counts in broad channels (from one-third to one-half the energy resolution of the detector) used in the analysis.

Channel number	Energy band, keV	Channel number	Energy band, keV
1	0.16 – 0.20	8	0.87 – 1.04
2	0.21 – 0.26	9	1.05 – 1.24
3	0.27 – 0.34	10	1.25 – 1.46
4	0.35 – 0.44	11	1.47 – 1.69
5	0.45 – 0.56	12	1.70 – 1.93
6	0.57 – 0.70	13	1.94 – 2.23
7	0.71 – 0.86		

Table 2: Data on sources and observations used

Object	Observation	α	δ	Count rate, phot/s	Off-axis angle
RX J0439.8-6809	rp400161n00	04 ^h 39 ^m 49 ^s 6	-68°09'01"	1.40	1.'52
RX J0513.9-6951	rp900398a02	05 ^h 13 ^m 48 ^s 8	-69°52'00"	1.947	0.57
RX J0527.8-6954	rp400148n00	05 ^h 27 ^m 48 ^s 6	-69°54'02"	0.1171	0.061
CAL 87	rp400012n00	05 ^h 46 ^m 45 ^s 0	-71°08'54"	0.121	0.1
CAL 83	rp110180n00	05 ^h 43 ^m 33 ^s 5	-68°22'23"	0.53	40.29
1E 0035.4-7230	rp400299n00	00 ^h 37 ^m 19 ^s 0	-72°14'14"	0.52	0.167
	rp400149n00			0.41	0.167
RX J0048.4-7332	rp600196a01	00 ^h 48 ^m 20 ^s 0	-73°31'55"	0.17	20.87
1E 0056.8-7154	rp600455a02	00 ^h 58 ^m 37 ^s 1	-71°35'48"	0.325	18.3
	rp400300a01			0.373	0.38
RX J0019.8+2156	rp400322n00	00 ^h 19 ^m 50 ^s 1	+21°56'54"	1.96	0.103
RX J0925.7-4758	rp900377n00	09 ^h 25 ^m 42. ^s 0	-47°58 ^m 00 ^s	0.675	40.99
AG Draconis	rp200689n00	16 ^h 01 ^m 41. ^s 1	+66°48'10"	1.09	1.88

Table 3: Approximation parameters for the minimum $\log g$.

Object	N_H , 10^{20} cm $^{-2}$	T_{eff} , $\times 10^5$ K	$\log g$ cm s $^{-2}$	$\log (R/d)^2$	Flux (0.2-2 keV) erg cm $^{-2}$ s $^{-1}$	χ^2 / d.o.f.	Type of errors
RX J0439	$4.75^{+10.15}_{-4.67}$	$2.80^{+1.52}_{-0.70}$	7.5	$-26.63^{+5.29}_{-2.84}$	$4.32 \cdot 10^{-11}$	9.30/8	A
RX J0513	$5.94^{+0.47}_{-0.40}$	$5.95^{+0.10}_{-0.07}$	$8.4^{+0.04}_{-0.15}$	$-28.57^{+0.10}_{-0.08}$	$1.09 \cdot 10^{-10}$	19.4/8	C
RX J0527	$27.6^{+11.3}_{-24.25}$	$3.02^{+2.49}_{-1.81}$	8.0	$-23.43^{+10.0}_{-6.65}$	$1.26 \cdot 10^{-7}$	1.47/8	A
CAL 87	$69.2^{+23.1}_{-22.0}$	$8.20^{+0.22}_{-0.24}$	9.0	$-28.20^{+0.85}_{-0.81}$	$1.17 \cdot 10^{-9}$	13.5/8	C
CAL 83	$11.0^{+11.3}_{-6.46}$	$4.64^{+0.94}_{-0.64}$	8.0	$-27.59^{+2.17}_{-1.51}$	$2.62 \cdot 10^{-10}$	16.1/8	B
1E 0035	$5.00^{+3.72}_{-2.34}$	$4.82^{+0.49}_{-0.29}$	8.0	$-28.89^{+0.80}_{-0.63}$	$1.67 \cdot 10^{-11}$	6.69/8	C
	$3.83^{+3.13}_{-1.89}$	$4.96^{+0.54}_{-0.34}$	8.0	$-29.29^{+0.74}_{-0.56}$	$8.16 \cdot 10^{-12}$	3.42/8	C
RX J0048	$27.6^{+10.5}_{-12.6}$	$3.35^{+0.55}_{-0.48}$	7.5	$-24.55^{+2.82}_{-2.50}$	$3.09 \cdot 10^{-8}$	8.08/8	C
1E 0056	$12.1^{+7.00}_{-9.24}$	$2.69^{+0.95}_{-0.43}$	7.5	$-25.01^{+1.37}_{-3.82}$	$1.20 \cdot 10^{-9}$	9.41/8	A
	$3.71^{+21.29}_{-2.38}$	$4.00^{+1.24}_{-0.97}$	8.0	$-28.85^{+2.02}_{-0.44}$	$5.31 \cdot 10^{-12}$	13.2/8	B
RX J0019	$16.7^{+6.9}_{-13.35}$	$2.80^{+1.26}_{-0.35}$	7.5	$-23.62^{+2.82}_{-4.67}$	$4.46 \cdot 10^{-8}$	18.1/8	A
RX J0925	163^{+14}_{-46}	$9.85^{+1.05}_{-0.37}$	9.5	$-26.23^{+0.59}_{-1.57}$	$2.53 \cdot 10^{-7}$	8.85/8	C
AG Dra	$0.0595^{+0.0405}_{-0.0595}$	$3.09^{+0.41}_{-2.59}$	7.5	$-28.82^{+14.82}_{-0.18}$	$7.67 \cdot 10^{-13}$	4.21/8	B

Note: Fluxes have been corrected for interstellar absorption.

Type of errors: A denotes error limits based on the limiting values of N_H (98%);

B denotes error limits based on the left boundary of N_H and $2N_H$ for the best approximation (98%);

C denotes errors derived from usual χ^2 criteria (90%). The error for $\log g$ for RXJ0513 is 1σ ;

the remaining parameters were derived with this value fixed. The data for AG Dra are approximate.

Table 4: Approximation parameters for the maximum $\log g$.

Object	N_H , 10^{20} cm^{-2}	T_{eff} , $\times 10^5 \text{ K}$	$\log g$ cm s^{-2}	$\log (R/d)^2$	Flux (0.2-2 keV) $\text{erg cm}^{-2} \text{ s}^{-1}$	$\chi^2/\text{d.o.f.}$	Type of errors	
RX J0439	$5.00^{+0.06}_{-5.00}$	$3.10^{+2.75}_{-0.88}$	9.5	$-26.79^{+1.81}_{-3.31}$	$5.03 \cdot 10^{-11}$	9.31/8	A	
RX J0513				Not presented: one possible value of $\log g$				
RX J0527	$21.9^{+8.00}_{-18.55}$	$3.43^{+3.62}_{-0.22}$	9.5	$-25.10^{+2.03}_{-5.52}$	$6.72 \cdot 10^{-9}$	1.47/8	A	
CAL 87				Not presented: one possible value of $\log g$				
CAL 83	$10.6^{+24.4}_{-6.25}$	$5.65^{+1.48}_{-1.08}$	9.5	$-28.11^{+2.19}_{-1.51}$	$2.16 \cdot 10^{-10}$	16.3/8	B	
1E 0035	$4.62^{+3.54}_{-2.21}$	$5.93^{+0.75}_{-0.50}$	9.5	$-29.4^{+0.85}_{-0.65}$	$1.44 \cdot 10^{-11}$	6.61/8	C	
	$3.51^{+2.97}_{-1.77}$	$6.14^{+0.82}_{-0.53}$	9.5	$-29.79^{+0.72}_{-0.56}$	$7.23 \cdot 10^{-12}$	3.44/8	C	
RX J0048	$22.7^{+5.1}_{-9.2}$	$4.10^{+0.90}_{-0.63}$	9.5	$-25.88^{+1.71}_{-0.81}$	$5.21 \cdot 10^{-9}$	9.35/8	C	
1E 0056	$10.1^{+4.10}_{-8.07}$	$3.00^{+1.96}_{-0.56}$	9.5	$-25.81^{+2.46}_{-3.96}$	$3.35 \cdot 10^{-10}$	9.82/8	A	
	$3.28^{+17.42}_{-2.21}$	$4.59^{+1.97}_{-1.24}$	9.5	$-29.29^{+1.95}_{-1.20}$	$4.26 \cdot 10^{-12}$	13.1/8	B	
RX J0019	$11.7^{+6.20}_{-8.76}$	$3.31^{+2.04}_{-0.60}$	9.5	$-25.40^{+2.81}_{-3.57}$	$2.39 \cdot 10^{-9}$	18.2/8	A	
RX J0925				Not presented: one possible value of $\log g$				
AG Dra	$2.51^{+3.99}_{-2.51}$	$1.16^{+2.84}_{-0.66}$	9.5	$-20.96^{+4.66}_{-8.36}$	$3.49 \cdot 10^{-12}$	4.20/8	A	

Note: See comments to Table 3.

Table 5: Approximation parameters for the minimum $\log g$ and Galactic N_H .

Object	N_H , 10^{20} cm^{-2}	T_{eff} , $\times 10^5 \text{ K}$	$\log g$ cm s^{-2}	$\log (R/d)^2$	Flux (0.2-2 keV) $\text{erg cm}^{-2} \text{ s}^{-1}$	$\chi^2/\text{d.o.f.}$
RX J0439	5.60	$2.72_{-0.15}^{+0.12}$	7.5	$-26.24_{-0.26}^{+0.35}$	$7.99 \cdot 10^{-11}$	9.30/9
RX J0513	7.24	$5.74_{-0.03}^{+0.03}$	8.4	$-28.29_{-0.01}^{+0.02}$	$1.71 \cdot 10^{-10}$	33.8/9
RX J0527	6.31	$4.65_{-1.12}^{+0.24}$	8.0	$-29.18_{-0.09}^{+0.83}$	$6.90 \cdot 10^{-12}$	2.17/9
CAL 87	7.58	Unsatisfactory approximation				
CAL 83	6.33	$5.04_{-0.17}^{+0.17}$	8.0	$-28.57_{-0.08}^{+0.08}$	$4.59 \cdot 10^{-11}$	17.3/9
1E 0035	6.94	$4.64_{-0.11}^{+0.09}$	8.0	$-28.45_{-0.06}^{+0.06}$	$3.62 \cdot 10^{-11}$	7.58/9
	6.94	$4.64_{-0.13}^{+0.09}$	8.0	$-28.56_{-0.05}^{+0.08}$	$2.83 \cdot 10^{-11}$	6.10/9
RX J0048	4.24	Unsatisfactory approximation				
1E 0056	6.16	$2.90_{-0.11}^{+0.09}$	7.5	$-27.02_{-0.22}^{+0.26}$	$2.56 \cdot 10^{-11}$	10.3/9
	6.16	$3.20_{-0.09}^{+0.99?}$	8.0	$-27.63_{-0.86}^{+0.36}$	$1.85 \cdot 10^{-11}$	13.3/9
RX J0019	4.20	$3.57_{-0.20}^{+0.24}$	7.5	$-27.71_{-0.22}^{+0.20}$	$3.61 \cdot 10^{-11}$	19.5/9
RX J0925	55.6	Unsatisfactory approximation				
AG Dra	3.08	$2.35_{-0.16}^{+0.17}$	7.5	$-26.41_{-0.41}^{+0.46}$	$7.79 \cdot 10^{-12}$	4.73/9

Note: See comments to Table 3.

Table 6: Approximation parameters for the maximum $\log g$ and Galactic N_H .

Object	N_H , 10^{20} cm^{-2}	T_{eff} , $\times 10^5 \text{ K}$	$\log g$ cm s^{-2}	$\log (R/d)^2$	Flux (0.2-2 keV) $\text{erg cm}^{-2} \text{ s}^{-1}$	$\chi^2/\text{d.o.f.}$
RX J0439	5.60	$3.02^{+0.19}_{-0.20}$	9.5	$-26.47^{+0.37}_{-2.35}$	$7.77 \cdot 10^{-11}$	9.31/9
RX J0513	7.24			Not presented: one possible value of $\log g$		
RX J0527	6.31	$5.60^{+0.37}_{-1.68}$	9.5	$-29.59^{+0.95}_{-0.14}$	$6.84 \cdot 10^{-12}$	2.01/9
CAL 87	7.58			Not presented: one possible value of $\log g$		
CAL 83	6.33	$6.20^{+0.24}_{-0.25}$	9.5	$-29.01^{+0.09}_{-0.08}$	$4.59 \cdot 10^{-11}$	17.1/9
1E 0035	6.94	$5.61^{+0.14}_{-0.27}$	9.5	$-30.88^{+0.11}_{-0.06}$	$3.59 \cdot 10^{-11}$	7.95/9
	6.94	$5.60^{+0.14}_{-0.30}$	9.5	$-28.98^{+0.13}_{-0.06}$	$2.81 \cdot 10^{-11}$	6.83/9
RX J0048	4.24			Unsatisfactory approximation		
1E 0056	6.16	$3.31^{+0.16}_{-0.20}$	9.5	$-27.37^{+0.35}_{-0.29}$	$2.50 \cdot 10^{-11}$	10.3/9
	6.16	$3.65^{+0.87}_{-0.26}$	9.5	$-27.91^{+0.41}_{-0.77}$	$1.81 \cdot 10^{-11}$	13.3/9
RX J0019	4.20	$4.06^{+0.29}_{-0.17}$	9.5	$-28.01^{+0.14}_{-0.21}$	$3.47 \cdot 10^{-11}$	19.3/9
RX J0925				Not presented: one possible value of $\log g$		
AG Dra	3.08	$1.44^{+0.46}_{-0.23}$	9.5	$-22.49^{+1.46}_{-2.04}$	$5.24 \cdot 10^{-12}$	4.22/9

Note: See comments to Table 3.

Captions to figures

Figure 1. Difference between blanketed and unblanketed white-dwarf model atmospheres: (a) temperature structure (m is the column density), (b) spectra, and (c) spectra averaged over 10 eV. The model parameters are $T_{\text{eff}} = 500\,000$ K, $\log g = 8.5$, $A=1$. The solid curve shows the model with lines, while the dotted and dashed curves show the model without lines.

Figure 2. Atmospheric model spectra as functions of the (a) effective temperature ($\log g=8.5$, solar chemical composition, $T_{\text{eff}} = (1-9) \cdot 10^5$ K), (b) surface gravity ($T_{\text{eff}} = 5 \cdot 10^5$ K, solar chemical composition, $\log g=7.5 - 9.5$), and (c) chemical composition ($T_{\text{eff}} = 5 \cdot 10^5$ K, $\log g=8.5$, chemical compositions of 0.25, 0.5, and 1 of the solar value). The spectra are averaged over intervals of 10 eV.

Figure 3. Observed X-ray spectra for two of the studied sources together with the best-fitting theoretical spectra and the regions of admissible parameters in the $N_H - T_{\text{eff}}$ plane corresponding to the surface gravities chosen for the analysis (see Section 6). Values of the residuals are presented together with the spectra. The contours bound the 68, 90, and 99% probability zones, and the crosses mark the best-fit values. The source CAL 87 has a relatively hard spectrum, and its parameters are localized with certainty; CAL 83 has a soft spectrum, and the zone of allowed parameters in the $N_H - T_{\text{eff}}$ plane is very extended.

Figure 4. Comparison of derived parameters with the data of other studies (references given in the text): (a) effective temperatures and (b) column densities of interstellar hydrogen.

Figure 5. Position of the studied sources in the $T_{\text{eff}} - \log g$ plane. The bold solid curves show the strip of stable burning. The dotted curve indicates the Eddington limit.

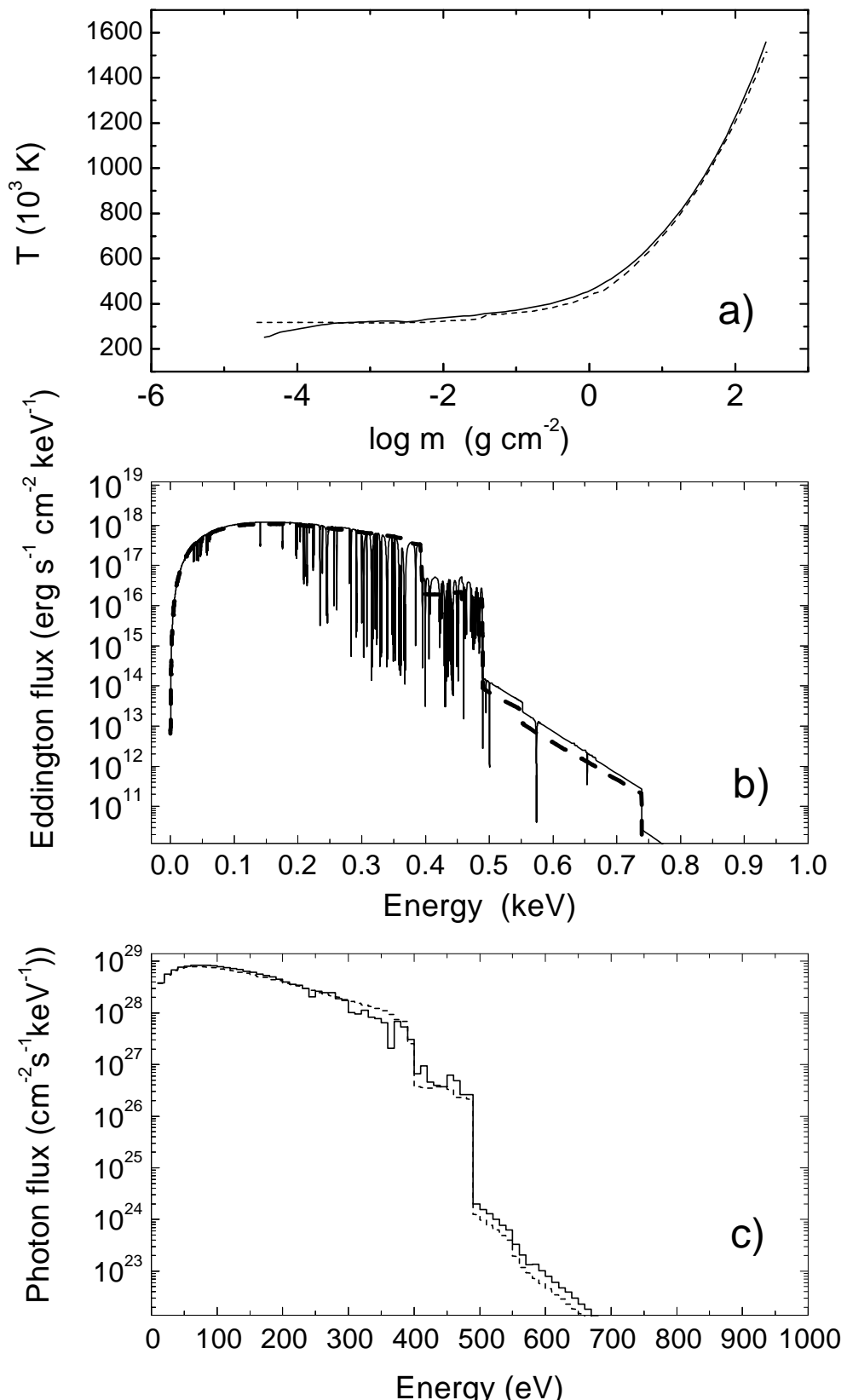


Figure 1:

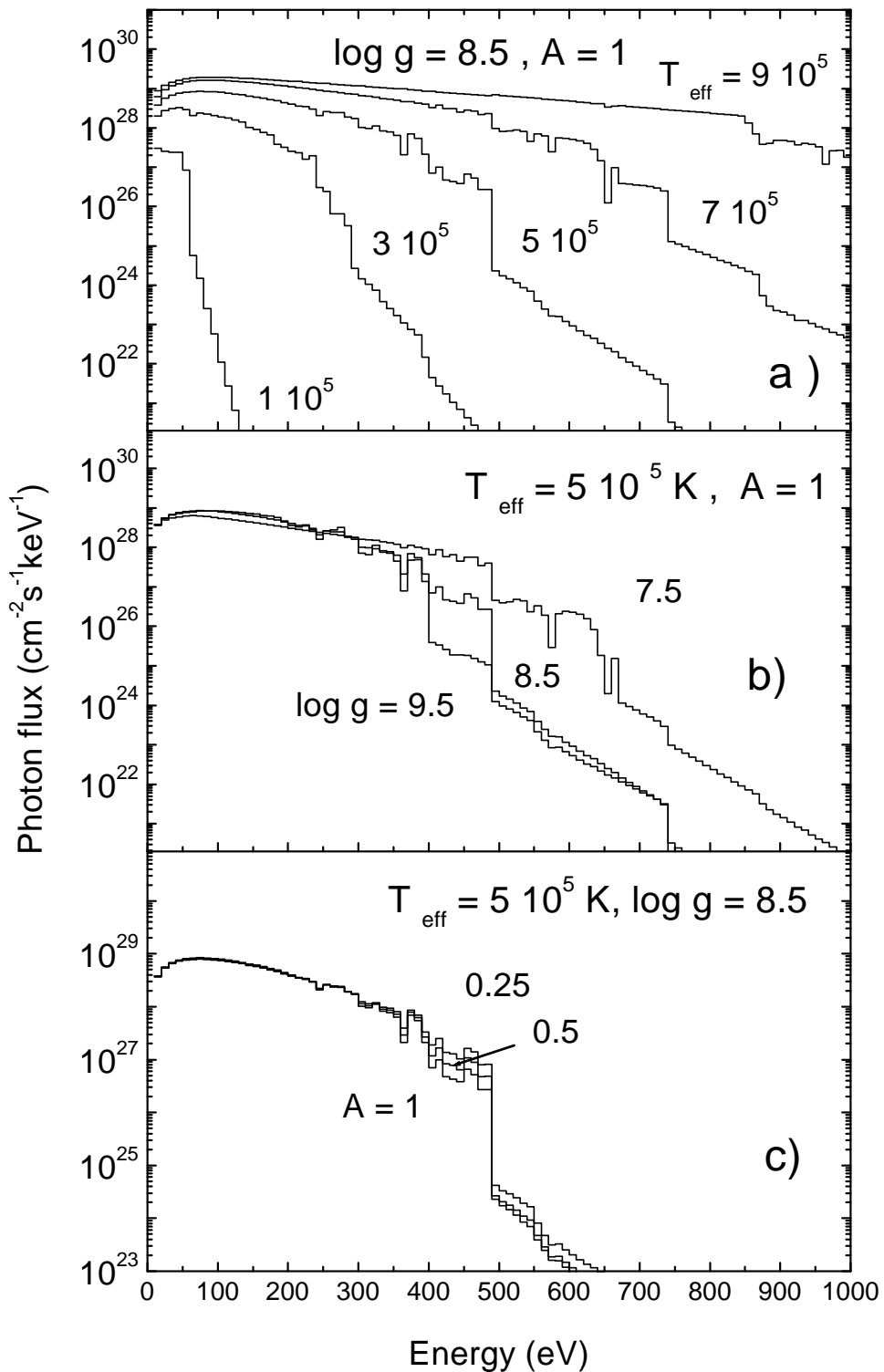


Figure 2:

Figure 3:

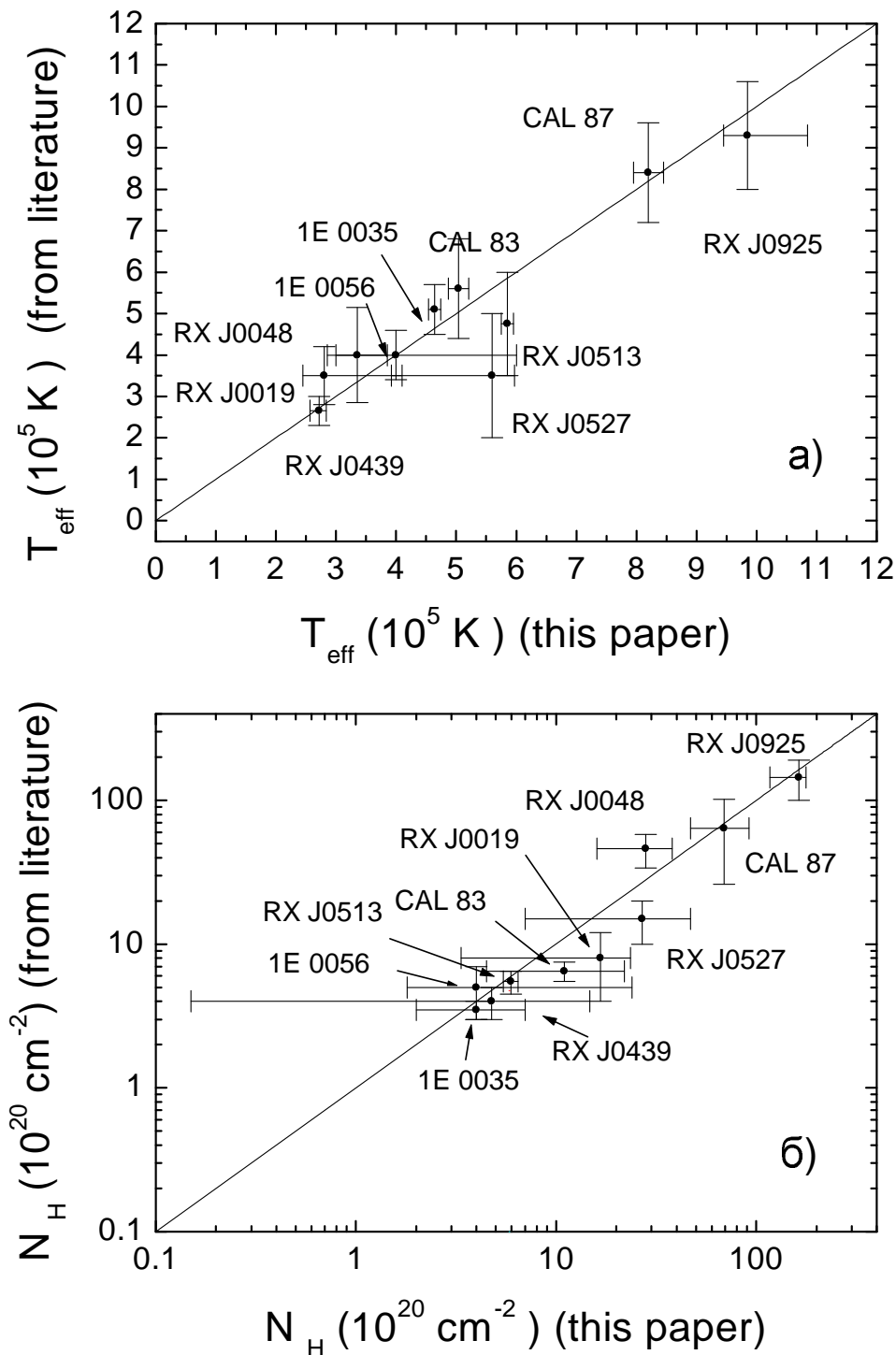


Figure 4:

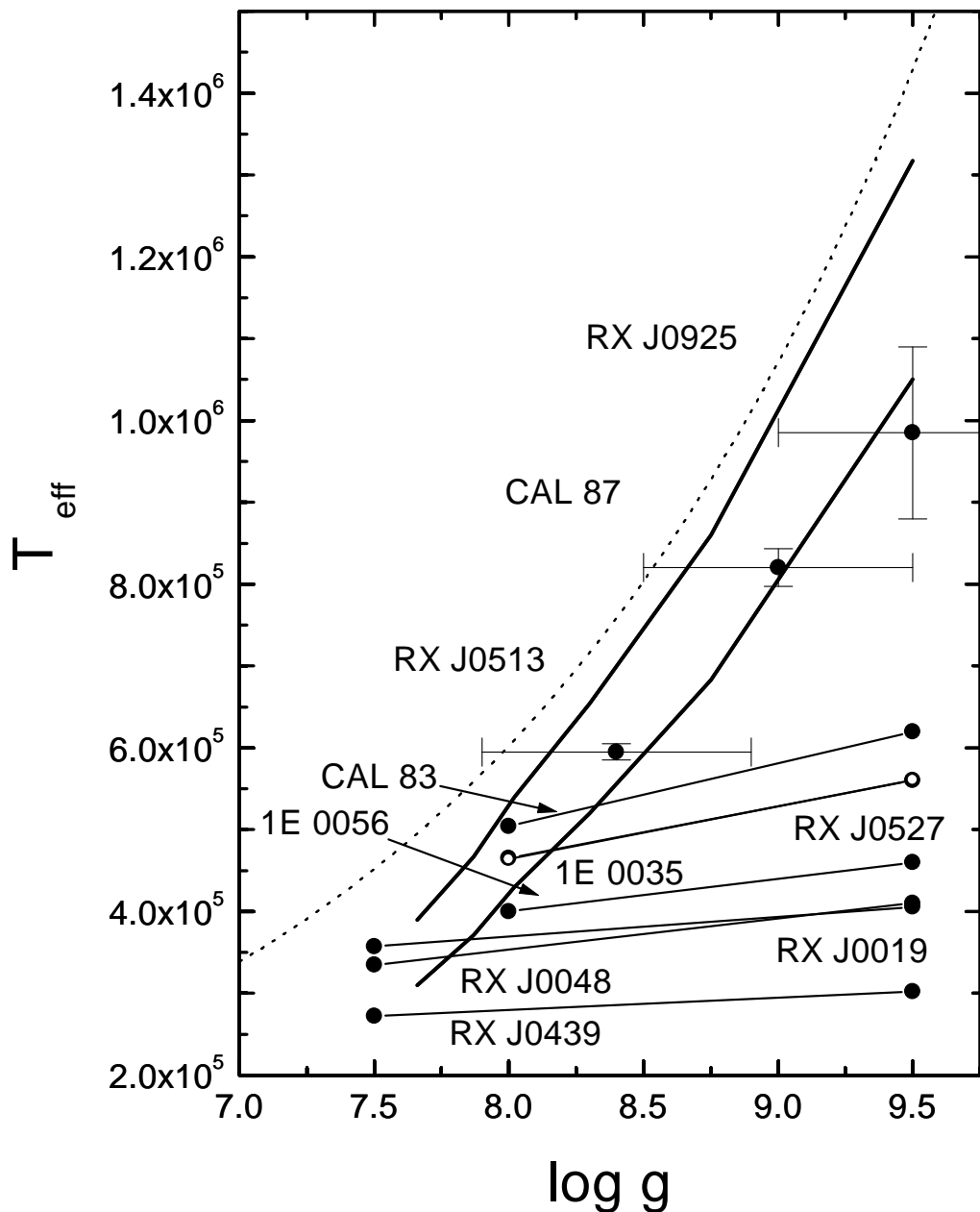
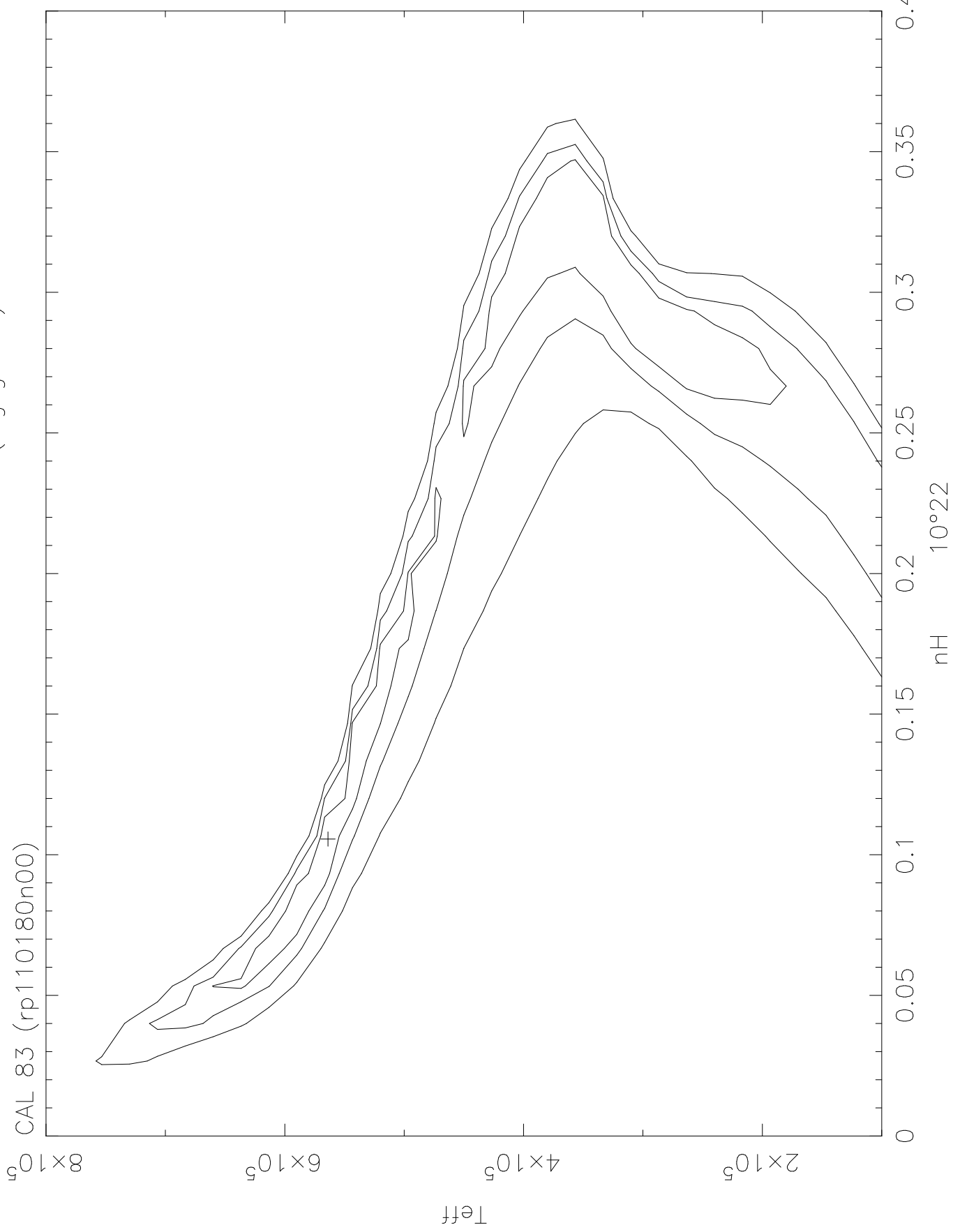
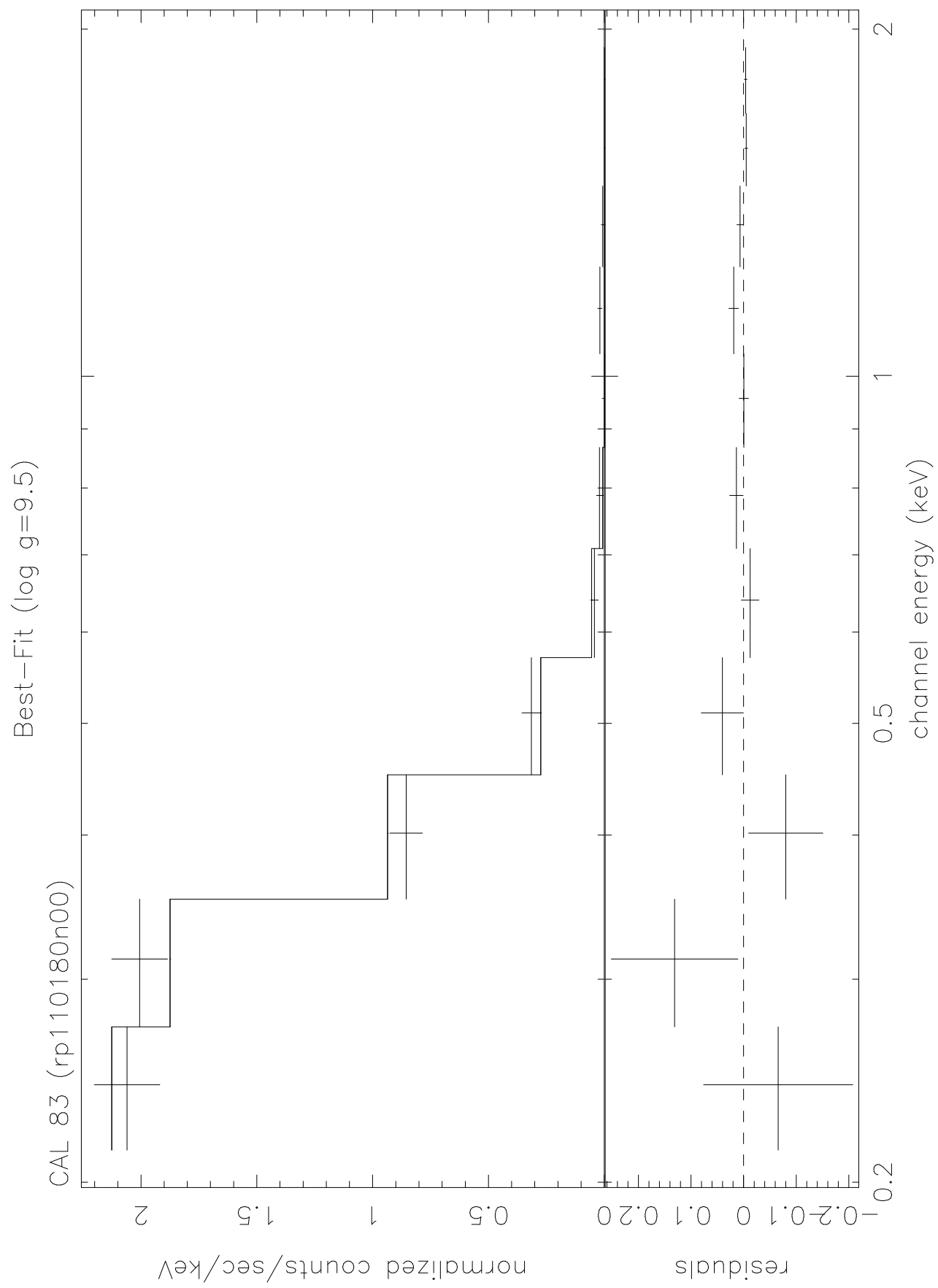


Figure 5:

Best-Fit confidence contours (log $g=9.5$)



root 29-Aug-2000 17:04



Best-Fit confidence contours ($\log g=9$)

CAL 87 (rp4000012n00)

T_{eff}

0.2

0.4

0.6

0.8

1

$10^{\circ}22$

nH

